Direct Numerical Simulations of Acoustic Disturbances in Various Rectangular Nozzle Configurations

Nathaniel Hildebrand* and Meelan M. Choudhari†
NASA Langley Research Center, Hampton, VA, 23681

Lian Duan‡
The Ohio State University, Columbus, OH, 43210

We perform Direct Numerical Simulations (DNS) to study the acoustic freestream disturbances radiating from the turbulent boundary layers along the contoured nozzle walls of a hypersonic wind tunnel with a rectangular test section. To begin with, the effects of the spanwise end walls are suppressed by confining the spanwise computational domain to a finite segment of the overall nozzle cross section and by imposing periodic boundary conditions across that spanwise domain. Besides providing a building-block configuration to reveal partial effects of the enclosed acoustic environment within the wind tunnel, these computations serve as a stepping stone toward the goal of fully-3D computations including the nozzle end walls. Building upon the earlier simulations of Deegan et al. (2018), we show that the computed acoustic characteristics in the spanwise periodic simulations are insensitive to changes in the grid resolution parameters (e.g., x^+ and z^+). This is relative to the previous simulations that involved a coarser resolution in the streamwise and wall-normal directions, especially upstream of the test section. Furthermore, we outline a comparison of the pressure fluctuations induced by the turbulent boundary layers over the contoured nozzle walls and several other calculations involving boundary layers over a single flat plate at nearly the same value of the edge Mach number. We also show the impact of having only one turbulent boundary layer instead of two within the computational setup. Various flow statistics, including the first and second moments of the unsteady flow field, are computed for the different flow configurations. Good comparisons of the statistics of the nozzle-wall boundary-layer turbulence and of the freestream acoustic disturbances between the simulations of coarser and finer grids confirms not only the adequacy of the DNS procedure, but also the insensitivity of noise characteristics in the test section to the inflow turbulence generation technique.

Nomenclature

a	speed of sound, m/s
C_f	skin-friction coefficient, dimensionless
c_p	coefficient of specific heat at constant pressure, J/(K·kg)
H	shape factor defined as δ^*/θ, dimensionless
L	length of the computational domain, m
M	Mach number, dimensionless
N	number of grid points, dimensionless
p	pressure, Pa
Pr	Prandtl number, dimensionless
R	ideal gas constant, J/(K·kg)
Re_{unit}	unit Reynolds number defined as $\rho_\infty U_\infty/\mu_\infty$, 1/m
Re_{δ^*}	Reynolds number based on the displacement thickness defined as $\rho_\infty U_\infty \delta^*/\mu_\infty$, dimensionless
Re_θ	Reynolds number based on the momentum thickness defined as $\rho_\infty U_\infty \theta/\mu_\infty$, dimensionless

*Aerospace Technologist, Computational AeroSciences Branch, AIAA Member
†Aerospace Technologist, Computational AeroSciences Branch, AIAA Fellow
‡Associate Professor, Mechanical and Aerospace Engineering Department, AIAA Senior Member

Re_τ	Reynolds number based on the shear velocity and the wall viscosity defined as $\rho_w u_\tau \delta / \mu_w$, dimensionless
T	temperature, K
T_r	recovery temperature defined as $T_\infty[1 + 0.45(\gamma - 1)M_\infty^2]$, K
U	magnitude of the velocity vector, m/s
(u, v, w)	streamwise, spanwise, and cross-stream velocity components, m/s
(x, y, z)	Cartesian coordinates, m
z_n	wall-normal distance, m
z_τ	viscous length defined as ν_w / u_τ, m
γ	specific heat ratio defined as c_p / c_v, dimensionless
δ	boundary-layer thickness based on 99% of the freestream velocity, m
δ^*	boundary-layer displacement thickness, m
θ	boundary-layer momentum thickness, m
κ	coefficient of thermal conductivity, W/(m·K)
μ	dynamic viscosity, kg/(m·s)
ρ	density, kg/m^3

Subscripts

in	inflow quantities
out	outflow quantities
w	wall quantities
∞	freestream quantities
min	minimum value
rms	root mean square
VD	van Driest transformation
TL	Trettel and Larsson transformation

Superscripts

$+$	viscous units
$*$	semilocal units
$'$	fluctuations around standard (Reynolds) averages
$''$	fluctuations around density-weighted (Favre) averages

I. Introduction

Laminar-turbulent transition in a boundary layer is accompanied by a several-fold increase in the skin-friction drag and heat flux to the wall [1]. As a result, uncertainties in transition prediction can have a substantial impact on the design of a hypersonic vehicle. Transition at flight altitudes is usually initiated by linear instabilities of the boundary-layer flow, which are excited via the receptivity of this flow to its disturbance environment. Even though the dominant sources of receptivity at flight altitudes are not known, experimental measurements have shown that testing in conventional (i.e., noisy) high-speed wind tunnels usually results in an earlier onset of transition relative to that in a flight environment. While low-disturbance (i.e., quiet) wind tunnels can usually mimic the in-flight transition characteristics, the currently available hypersonic quiet tunnels are limited in size, maximum quiet-flow Reynolds number, Mach number range, and maximum freestream enthalpy. Therefore, the aerothermodynamic testing of hypersonic vehicles must often be carried out in the conventional facilities.

The disturbance environment in a conventional high-speed wind tunnel includes a mix of acoustic, vortical, and entropy disturbances, along with any particulates from the incoming flow. A main source of acoustic disturbances consists of turbulent eddies in the high-speed boundary layers along the walls of the wind tunnel nozzle [2]. As the freestream Mach number increases, the intensity of these acoustic disturbances becomes much stronger. Hence, they often dominate the overall disturbance environment (as opposed to the vorticity or entropy disturbances) at Mach numbers of 2.5 or above [3–6]. To allow for a better use of the high-speed transition data from the conventional facilities, it is important to understand the acoustic fluctuation field that dominates the freestream disturbance environment. Also, with an increased knowledge base of the various receptivity mechanisms in high-speed boundary layers [7, 8], it becomes more important to characterize the details of the acoustic field in conventional wind tunnels so that the

receptivity theories may be applied toward the understanding and prediction of transition behavior (in these tunnels). This characterization would also help extrapolate from the wind tunnel measurements to flight.

Direct Numerical Simulations (DNS) of the acoustic fluctuation field radiated from high-speed turbulent boundary layers along the wind-tunnel walls are able to overcome several difficulties encountered during experimental measurements [9]. DNS also provides access to flow quantities that cannot be measured easily [10, 11]. The successful application of DNS for capturing acoustic pressure fluctuations radiated from high-speed turbulent boundary layers is first demonstrated in [9, 12–14], which investigated spatially-developing turbulent boundary layers over a flat plate at Mach 2.5-14. These simulations isolated the acoustic radiation from a single surface, thus facilitating a comprehensive understanding of the origin of the freestream disturbance environment and its dependence on boundary-layer parameters (such as edge Mach number, wall temperature, and local Reynolds number). DNS has also been applied to investigate the acoustic radiation from turbulent boundary layers developing along the inner walls of an axisymmetric nozzle [15, 16]. These simulations permitted the characterization of noise generation and reverberation within an axisymmetric nozzle.

Many operating hypersonic wind tunnels (including the NASA 20-Inch Mach 6 Wind Tunnel) have a rectangular test section, and therefore, are nonaxisymmetric in nature [17]. The freestream disturbances in these tunnels represent the net effect of acoustic radiation from the boundary layers along the four nozzle walls and the corner flows in between. The spatio-temporal characteristics of freestream disturbances within a rectangular test section are determined by the outcome of the acoustic reverberation process within the confined environment, and the nature of this reverberation in a nonaxisymmetric nozzle is expected to be different from that inside an axisymmetric wind tunnel. To further understand the wind-tunnel acoustic environment in nonaxisymmetric nozzles, the current research effort seeks to simulate the acoustic radiation within a rectangular nozzle. It is also an extension of the earlier work by Deegan et al. [17], which presented preliminary simulations of the acoustic radiation in a quasi-2D nozzle (similar to the convergent-divergent nozzle from the NASA 20-Inch Mach 6 Wind Tunnel, but without the two spanwise end walls). The current work seeks to extend the computations presented in Ref. [17] via additional simulations of the quasi-2D configuration as well as by studying the effect of having only one turbulent boundary layer (on the bottom nozzle wall) inside the rectangular test section instead of two (on the top and bottom nozzle walls).

By suppressing the effects of the spanwise end walls and the corners in between them on the acoustic noise generation and reverberation processes, the simpler quasi-2D flow configuration provides a useful reference toward characterizing the effects of the individual wind-tunnel walls on the overall acoustic disturbance field. Furthermore, from a numerical standpoint, it provides a less expensive means of refining and fine tuning the simulation process for the eventual fully-3D simulation that includes the end walls.

II. Problem Formulation

A. Flow Configuration

In the current research effort, we consider turbulent flow in a quasi-2D flow configuration of a rectangular nozzle test section. The Reynolds-Averaged Navier-Stokes (RANS) equations are used to simulate the full geometry (refer to Deegan et al. [17]), including the converging and diverging nozzle sections that lead up to the main test section of a representative wind tunnel. DNS is only used to simulate the diverging section of the wind tunnel nozzle. Figure 1 shows a spanwise slice of time-averaged Mach number contours from the DNS. Notice that the DNS computational domain starts slightly downstream of the nozzle throat at $x = 0.305$ m and extends to the nozzle exit at $x = 3.67$ m. From the given streamwise domain length, and the well-known rapid growth of acoustic radiation with increasing Mach number at the boundary-layer edge, we believe that the selected computational domain for the DNS encompasses the origin of a vast majority of the acoustic sources responsible for generating the freestream noise inside the rectangular nozzle test section [17].

To anchor the tunnel conditions to a relevant flow configuration, we consider flow conditions that fall within the operating range of the NASA 20-Inch Mach 6 Wind Tunnel. The wall temperature is 300 K, corresponding to a wall-to-recovery temperature ratio of $T_w/T_r \approx 0.64$. Here, the freestream Mach number, velocity, temperature, and density are $M_\infty = 5.97$, $U_\infty = 948$ m/s, $T_\infty = 64.3$ K, and $\rho_\infty = 0.033$ kg/m^3, respectively. The unit Reynolds number in this simulation is 2×10^6/m. Furthermore, the boundary-layer thickness at the nozzle exit ($x = 3.67$ m) is equal to $\delta = 68.9$ mm. For additional boundary-layer properties, including the boundary-layer displacement thickness and shape factor, refer to Table 1. We utilize a Cartesian coordinate system with x, y, and z denoting the streamwise, spanwise, and cross-stream directions, respectively.

A major difference between the simulations in this work and those in Deegan et al. [17] is the computational grid. Figure 2 shows $x^+ = x/z_\tau$ and $z^+ = z/z_\tau$ as functions of x along the bottom wall for the current grid employed in this

study and for the baseline grid taken from Ref. [17]. Notice that the current grid has much smaller values of x^+ and z^+ than the baseline grid, particularly from $x = 0.5$ m to $x = 2.5$ m. Since a portion of the acoustic fluctuations in the downstream region of interest may have been generated in the upstream regions, it is important to assess the effect of a finer wall-normal spacing on the acoustic fluctuations. A total of $N_x = 5630$, $N_y = 400$, and $N_z = 1199$ grid points resolve the domain in the streamwise, spanwise, and cross-stream directions, respectively, for the current grid employed in this study. The peak in x^+ around $x = 3.5$ indicates the start of an extra region that is appended to the computational domain of the DNS in order to prevent the reflection of any acoustic disturbances produced by the outflow boundary condition back into the flow regime of interest [17]. In the spanwise direction, we employ constant grid spacing with a value of $y^+ = y/z_\tau = 5.39$. Table 2 compares a few of the domain and grid resolution parameters between the baseline case [17] and the current simulation.

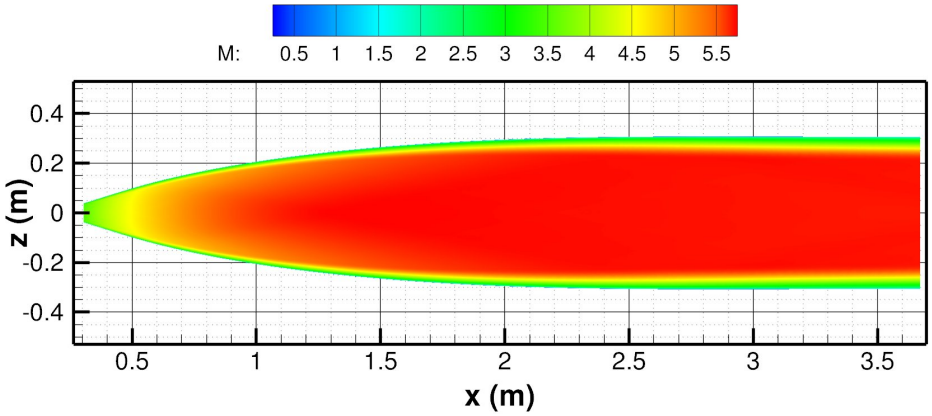

Fig. 1 Contours of time-averaged Mach number on a spanwise slice from the DNS of turbulent flow in a quasi-2D flow configuration of a rectangular nozzle test section. Similar to Deegan et al. [17], the nozzle shape has been nonuniformly distorted from its actual contour.

Table 1 Boundary-layer properties at the nozzle exit ($x = 3.67$ m) from the DNS, adapted from a recent conference paper by Deegan et al. [17].

M_∞	T_w (K)	T_w/T_r	Re_θ	Re_τ	Re_{δ^*}	δ (mm)	δ^* (mm)	H	z_τ (μm)	C_f (10^{-3})
5.97	300	0.64	28536	984	54680	68.9	27.34	6.69	69.5	7.8×10^{-4}

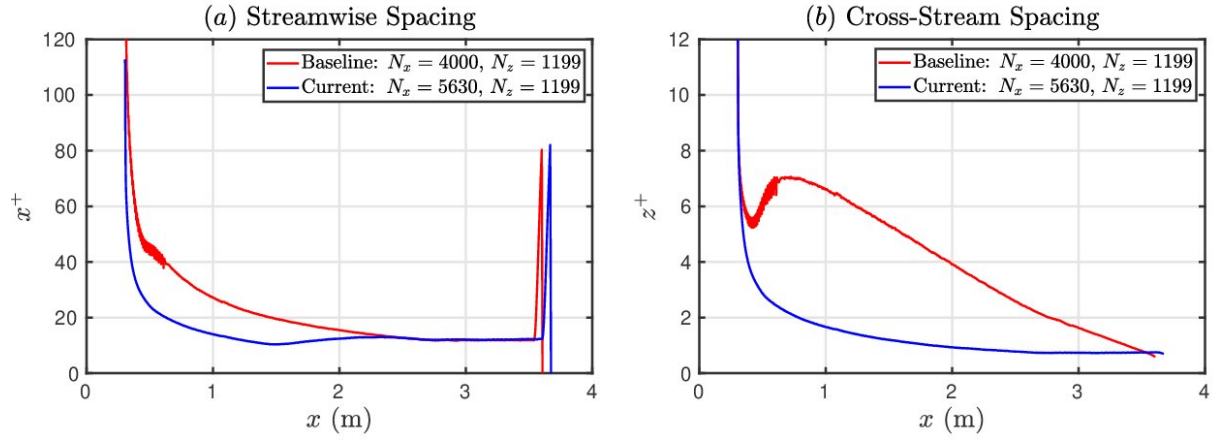

Fig. 2 Variations of (a) x^+ and (b) z^+ along the bottom nozzle wall for the current grid employed in this study and for the baseline grid taken from Deegan et al. [17].

Table 2 Domain and grid resolution parameters for the baseline simulation presented in Deegan et al. [17] and the current simulation presented in this work.

Grid	x_{in}	x_{out}	L_x	N_x	N_y	N_z	x^+_{min}	y^+	z^+_{w}	z^+_{∞}	L_x/δ_r
Baseline	0.305	3.67	3.27	4000	400	1199	11.61	5.39	1.07	7.44	47.8
Current	0.305	3.67	3.27	5630	400	1199	10.43	5.39	0.98	3.27	47.8

B. Numerical Methodology

The compressible three-dimensional Navier-Stokes equations in conservative form are solved numerically in curvilinear coordinates. They describe the spatio-temporal evolution of the system state, which consists of density, momentum, and total energy. We assume the fluid is a perfect gas and the usual constitutive relations for a Newtonian fluid hold: the viscous-stress tensor is linearly related to the rate-of-strain tensor and the heat-flux vector is linearly related to the temperature gradient through Fourier's law. The density ρ and temperature T are related to the pressure p through the equation of state $p = \rho RT$, where $R = 287.15$ J/(kg·K) is the specific gas constant for air. We compute the dynamic viscosity μ from Sutherland's law as such $\mu(T) = c_1 T^{1.5}/(T + T_s)$. The constants in Sutherland's law are set to the values of $c_1 = 1.458 \times 10^{-6}$ kg/(m·s·$\sqrt{\text{K}}$) and $T_s = 110.4$ K. Furthermore, the Prandtl number is set to $Pr = \mu c_p/\kappa = 0.71$, where c_p and κ are the coefficients of specific heat at constant pressure and thermal conductivity, respectively. We define the Mach number as $M = U/a$, where $a = \sqrt{\gamma p/\rho}$ is the speed of sound. Further, $\gamma = 1.4$ is the assumed constant ratio of specific heats.

A description of the governing equations can be found in Wu et al. [18]. The inviscid fluxes are modeled with a seventh-order Weighted Essentially Nonoscillatory (WENO) scheme. Instead of using the original finite-difference WENO scheme introduced by Jiang and Shu [19], we include limiters [20] to reduce the numerical dissipation. WENO adaption is limited to the boundary-layer region for maintaining numerical stability, while the optimal stencil of the WENO scheme is employed outside the boundary layer to achieve a higher resolution of the radiated acoustic field. We discretize the viscous fluxes via a central fourth-order finite-difference scheme. Time integration is performed with a third-order low-storage Runge-Kutta scheme [21].

For the inflow boundary condition, a digital-filter-based synthetic turbulence injection method is applied that generates correlated random fluctuations on nonuniform curvilinear meshes [22, 23]. The mean profiles, integral lengths, and Reynolds-stress tensor required for the digital filter are obtained from a precursor RANS computation that simulates the full wind-tunnel geometry [17]. No-slip boundary conditions are enforced for the three velocity components (streamwise, cross-stream, and spanwise) along the walls. An isothermal wall boundary condition is employed for the temperature. At the outflow boundary of the computational domain, an unsteady nonreflecting boundary condition based on Thompson [24] is utilized in conjunction with a fringe zone that has a streamwise stretched mesh to avoid acoustic reflections. Given the absence of end walls in the narrow-span computation, periodic boundary conditions are used in the spanwise direction.

III. Results

The simpler quasi-2D flow configuration allows for a characterization of the important effects of the individual wind-tunnel walls on the overall acoustic disturbance field within the wind tunnel. It also provides a less expensive way to refine and tune the simulation process for the eventual fully-3D simulation that includes the end walls. In this section, the current DNS results that are performed on a computational grid with $N_x = 5630$, $N_y = 400$, and $N_z = 1199$ are compared with the results of Ref. [17]. We also compute higher-order statistics and show the impact of having only one turbulent boundary layer instead of two inside the rectangular nozzle.

Figure 3 shows illustrative comparisons between the two DNS solutions by plotting the streamwise variation in the centerline Mach number and the boundary-layer thickness measured from the bottom wall. Part (a) in Figure 3 also shows the Mach number variation based on the isentropic approximation. The time-averaged DNS solution with the current grid is computed by using 82 instantaneous snapshots at intervals of 5.3×10^{-5} s. Notice that in part (b) of Figure 3 the boundary-layer thickness is a little smaller for the solution computed with the current grid than the solution computed with the baseline grid, specifically after $x = 2.0$ m. Nevertheless, the agreement of both the Mach number variation and the boundary-layer thickness between the two DNS solutions is relatively good. We show the

mean boundary-layer profiles at three selected streamwise stations (x = 1 m, x = 2 m, and x = 3 m) in Figure 4. These boundary-layer profiles correspond to the Mach number variation along the surface-normal direction, extending from the bottom nozzle wall to just short of the tunnel centerline. Comparisons between the mean profiles obtained from both DNS solutions indicate good agreement.

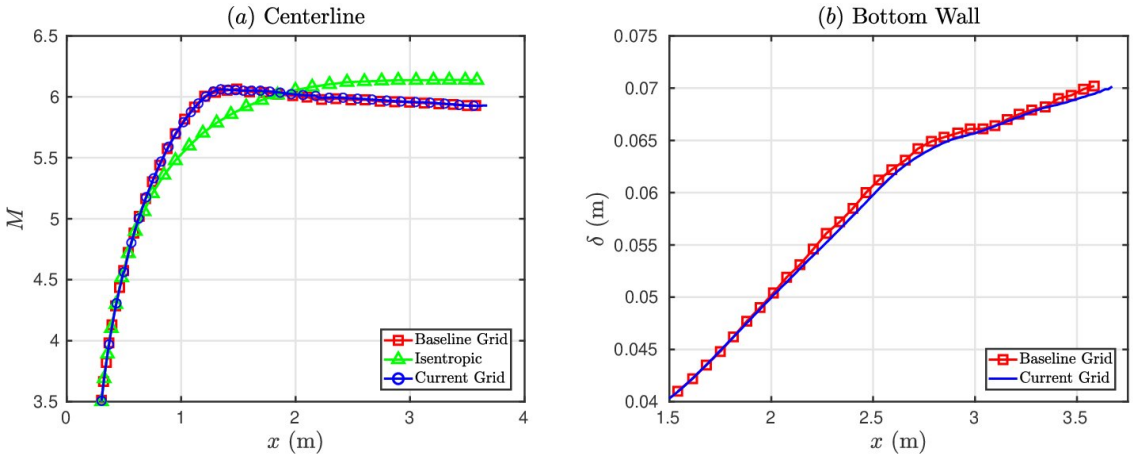

Fig. 3 Comparisons of the (a) streamwise Mach number variation at z = 0 m for the baseline and current simulations as well as for a 1D isentropic approximation and of the (b) boundary-layer thickness measured from the bottom wall in the streamwise direction for the baseline and current simulations.

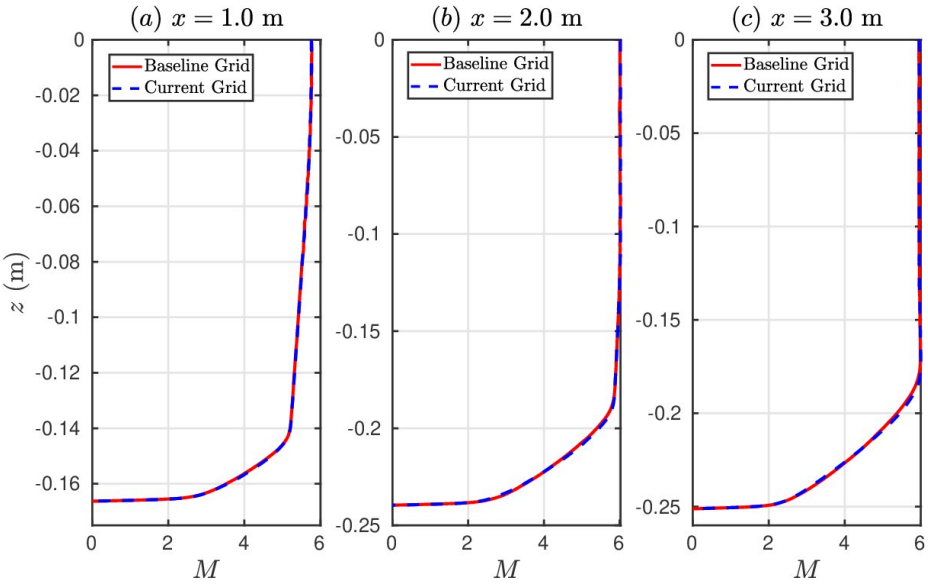

Fig. 4 Boundary-layer profile comparisons (in terms of Mach number) along the cross-stream direction for two time-averaged DNS solutions on the baseline and current grids. The profiles are extracted at three streamwise positions: (a) x = 1 m, (b) x = 2 m, and (c) x = 3 m.

Comparisons of the wall-normal profiles of the Reynolds stresses between the two time-averaged DNS solutions with different grids are depicted in Figure 5. All of the different components agree quite well between the two DNS solutions. In addition to comparing the Reynolds-averaged stresses between the two time-averaged DNS solutions with different grids, we also compare them to the Favre-averaged stresses in Figure 6 for the current grid described in Section II.A. Notice that the Reynolds- and Favre-averaged stresses are similar to one another at three different streamwise locations (x = 1.5 m, x = 2.5 m, and x = 3.5 m). The largest difference between the two types of averaging occurs for

the shear stresses close to the nozzle wall. It is important to note that the Reynolds- and Favre-averaged stresses are nearly identical in the freestream, but are not shown for conciseness.

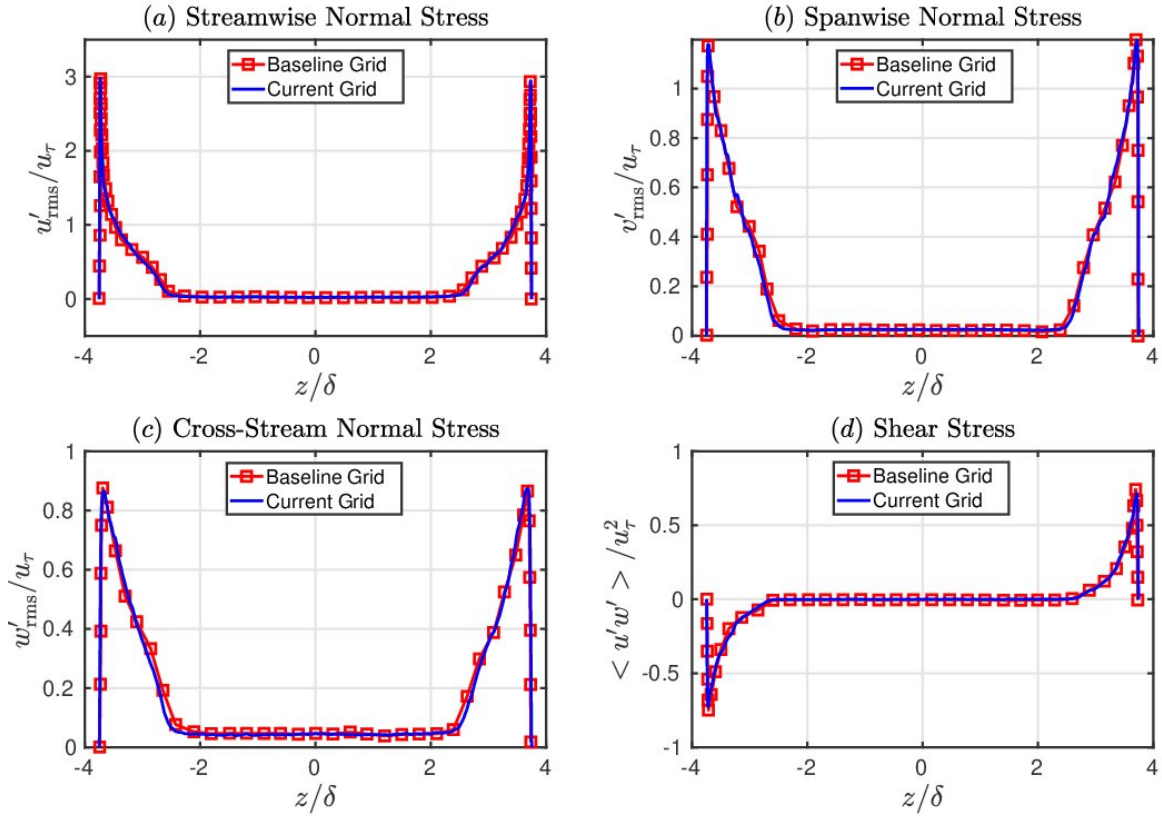

Fig. 5 Comparisons of the Reynolds stresses (a) u'_{rms}/u_τ, (b) v'_{rms}/u_τ, (c) w'_{rms}/u_τ, and (d) $<u'w'>/u_\tau^2$ along the cross-stream direction at a fixed streamwise position of x = 3.3 m for two time-averaged DNS solutions on the baseline and current grids.

We plot the van Driest transformed mean velocity u^+_{VD} versus z^+ in part (a) of Figure 7 from a quasi-2D nozzle DNS solution with the current grid described in Section II.A and several flat-plate calculations [9, 14, 25] at similar freestream Mach numbers. The van Driest transformed mean velocity is defined as

$$u^+_{VD} = \int_0^{u^+} (\bar{\rho}/\bar{\rho}_w)^{1/2} du^+, \tag{1}$$

where $u^+ = \bar{u}/u_\tau$ from [26]. We see that in part (a) of Figure 7 the slope of u^+_{VD} between the nozzle and flat-plate cases agrees quite well in the linear viscous sublayer and in the log layer. Notice that the values of u^+_{VD} in the boundary layer are larger for the nozzle simulation than for the different flat-plate cases. This is because Re_τ is greater in our nozzle simulation than in the other cases. We also perform an alternative transformation of the mean velocity proposed by Trettel and Larsson [27]. In this transformation, the velocity scaling is defined as

$$u^+_{TL} = \int_0^{u^+} \left(\frac{\bar{\rho}}{\bar{\rho}_w}\right)^{1/2} \left[1 + \frac{1}{2\bar{\rho}}\frac{d\bar{\rho}}{dz}z - \frac{1}{\bar{\mu}}\frac{d\bar{\mu}}{dz}z\right] du^+. \tag{2}$$

We plot u^+_{TL} versus z^* in part (b) of Figure 7, where $z^* = \rho z(\tau_w/\rho)^{1/2}/\mu$ from [28]. The transformation by Trettel and Larsson [27] shows an improved collapse of the data within the viscous sublayer region. Therefore, it performs slightly better than the van Driest transformation. Notice that the profile at x = 1.5 m from the quasi-2D nozzle DNS solution does not agree as well with the flat-plate calculations as the profile at x = 3.3 m. The nozzle cross section is still changing at x = 1.5 m. Thus, the boundary-layer flow is subject to a modest pressure gradient at this station.

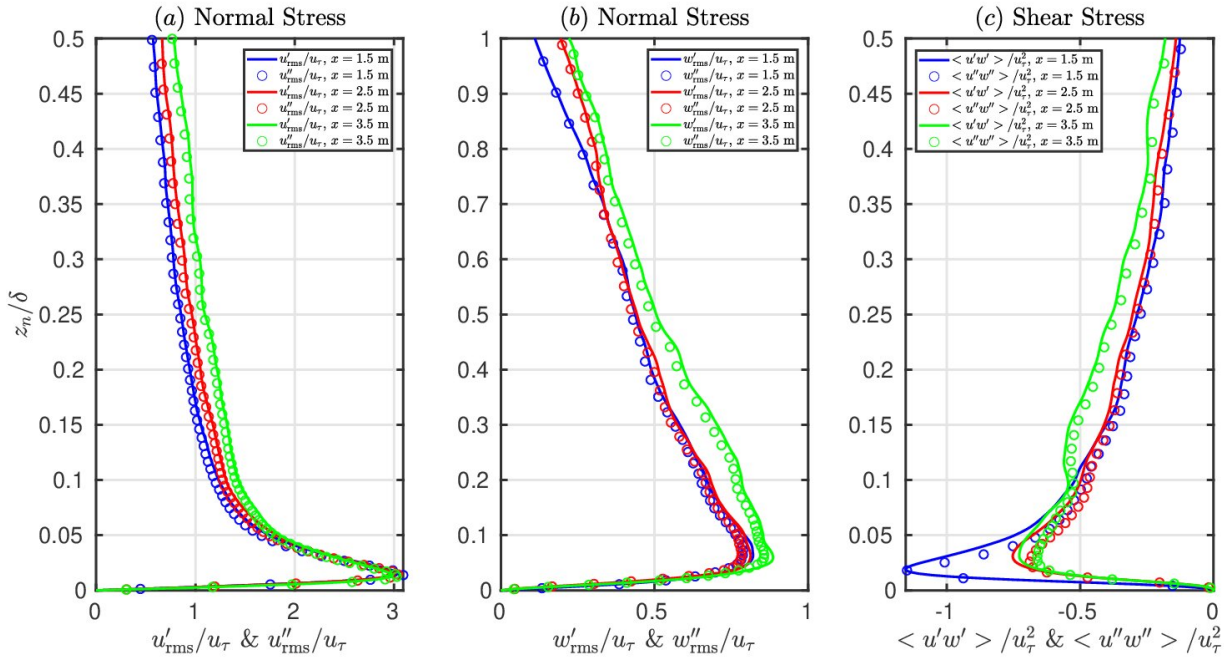

Fig. 6 Comparisons of the Favre-averaged (q'') and Reynolds-averaged (q') profiles of the normal and shear stresses at $x = 1.5$ m, $x = 2.5$ m, and $x = 3.5$ m from the quasi-2D nozzle DNS solution with the current grid: (a) u'_{rms}/u_τ and u''_{rms}/u_τ, (b) w'_{rms}/u_τ and w''_{rms}/u_τ, and (c) $< u'w' > /u_\tau^2$ and $< u''w'' > /u_\tau^2$.

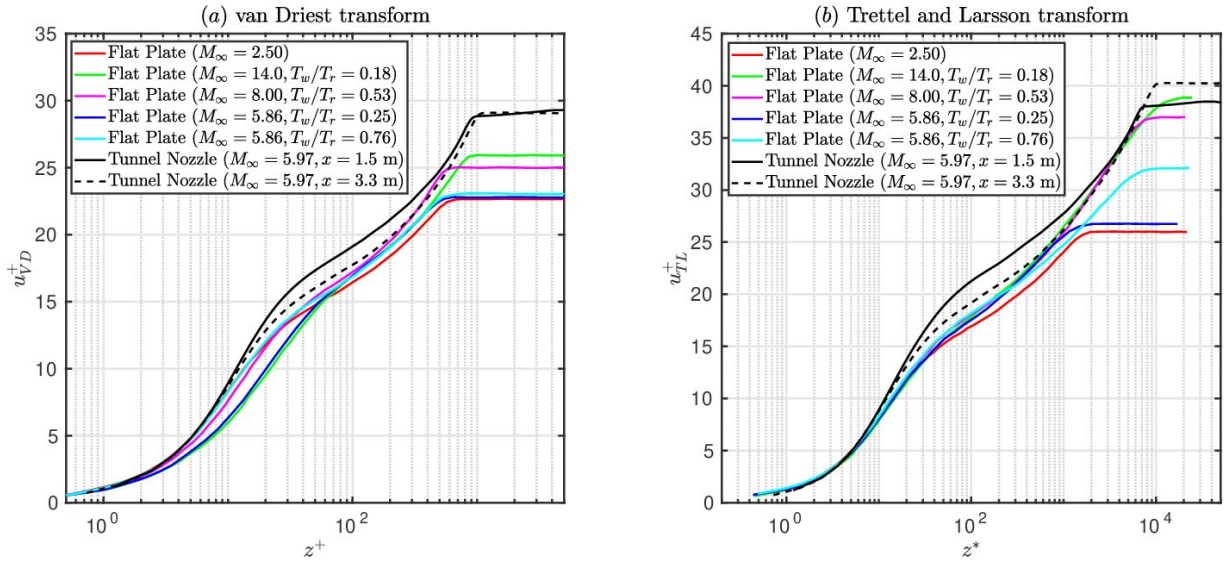

Fig. 7 Effect of applying the (a) van Driest transformation [26] and the (b) Trettel and Larsson transformation [27] to several mean velocity profiles from a quasi-2D nozzle DNS solution with the current grid described in Section II.A and several flat-plate calculations [9, 14, 25] at similar freestream Mach numbers.

Since we have established that the hydrodynamic characteristics of the turbulent boundary layer remain virtually unchanged between the two DNS solutions with different grids, we next compare the associated pressure fluctuations, both within the boundary layer and inside the nozzle core (i.e., freestream) regions. Figure 8 shows the cross-stream variation of the root-mean-square pressure fluctuation field divided by the freestream pressure for two quasi-2D nozzle DNS solutions with different grids at three streamwise locations. We see from Figure 8 that the solutions corresponding

to the current grid have small oscillations, which are likely due to averaging over a limited number of instantaneous snapshots (i.e., 82). Nevertheless, the agreement between the two quasi-2D nozzle DNS solutions is quite good considering the significant changes in x^+ and z^+ of the computational grids.

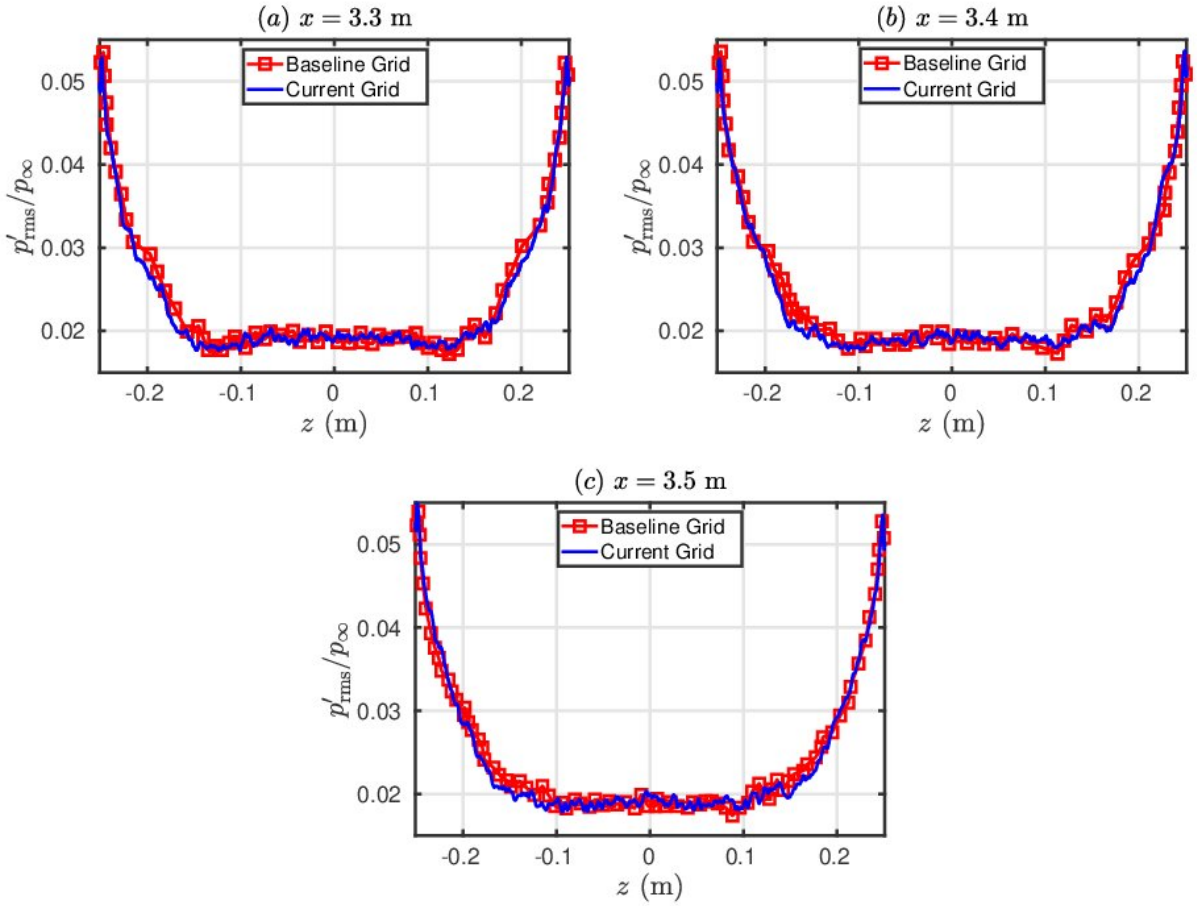

Fig. 8 Comparisons of p'_{rms}/p_∞ as functions of z between two quasi-2D nozzle DNS solutions with different grids at three streamwise locations: (a) x = 3.3 m, (b) x = 3.4 m, and (c) x = 3.5 m.

Figure 9 shows the cross-stream variation of the root-mean-square pressure fluctuation field divided by the wall shear stress induced by the turbulent boundary layer over the bottom nozzle wall for six different cases. Two of the six cases are the quasi-2D DNS solutions with different grids that have turbulent boundary layers on the top and bottom nozzle walls. Three other cases are from flat-plate calculations [9, 14, 25] at similar freestream Mach numbers (as the test section of the NASA 20-Inch Mach 6 Wind Tunnel). The last case corresponds to a quasi-2D nozzle DNS solution with just one turbulent boundary layer, which will be discussed later in this paper. We see from Figure 9 that the root-mean-square pressure fluctuation field is nearly homogeneous outside of the boundary layer (with a value of approximately 1.9% of the mean freestream pressure near the nozzle exit [17]). Furthermore, the intensity of pressure fluctuations within the freestream region is significantly larger in both nozzle simulations with two turbulent boundary layers than in the acoustic field induced by turbulent boundary-layer flow over a single flat plate. The increased acoustic intensity (that resides inside the nozzle) represents the combined effect of acoustic radiation from the top and bottom walls of the nozzle. Agreement between the pressure fluctuation statistics from the quasi-2D DNS solutions with different grids that have turbulent boundary layers on the top and bottom nozzle walls demonstrates that the acoustic field within the test section is nearly insensitive to fairly large changes in the computational grid. This key finding can be used to achieve a significant reduction in the computational cost of the full nozzle simulation including the nozzle end walls.

We show the power spectral density of acoustic fluctuations computed from two quasi-2D nozzle DNS solutions with different grids and two separate flat-plate calculations [9, 14, 25] in Figure 10. The power spectral density is computed about the centerline and x = 3.3 m in the nozzle simulations. Notice in Figure 10 there is relatively good

agreement between the two quasi-2D nozzle DNS solutions at lower frequencies. It is important to note that having more instantaneous snapshots would help smooth out the pressure spectra at lower frequencies. The pressure spectra start to diverge at higher frequencies because of the difference in grid resolution. Nevertheless, the close agreement between the nozzle and flat-plate data is very encouraging.

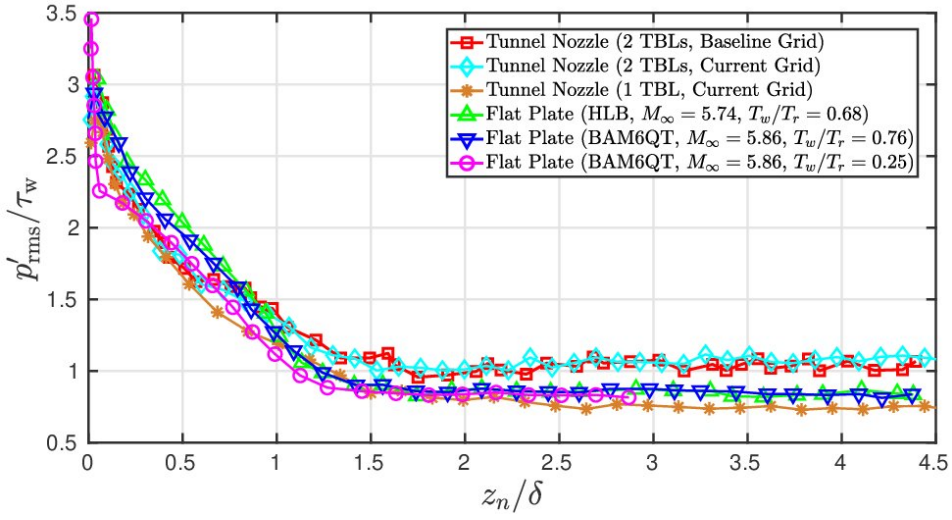

Fig. 9 Comparison of p'_{rms}/τ_w induced by the Turbulent Boundary Layer (TBL) over the bottom nozzle wall between three quasi-2D nozzle DNS solutions and three separate flat-plate calculations [9, 14, 25] at similar freestream Mach numbers. Here, z_n is the cross-stream distance from the bottom nozzle wall. The root-mean-square pressure profiles associated with the tunnel nozzle were extracted at x = 3.3 m.

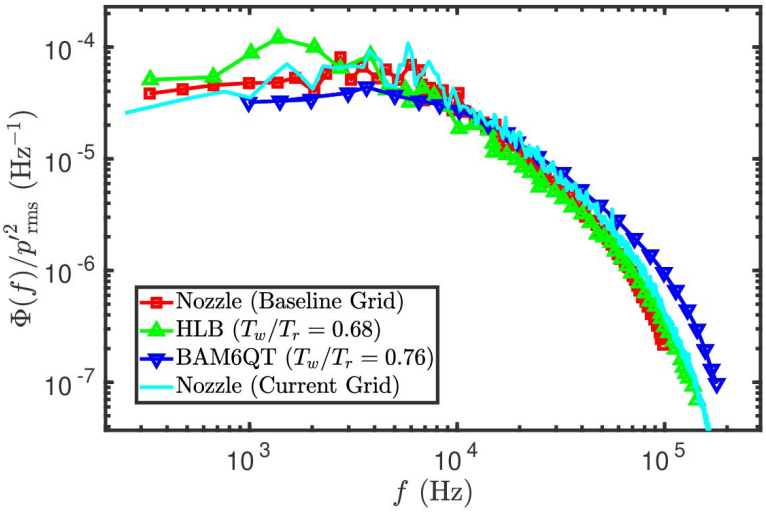

Fig. 10 Power Spectral Density (PSD) of freestream acoustic fluctuations versus frequency taken from two quasi-2D nozzle DNS solutions with different grids and two separate flat-plate calculations [9, 14, 25] at similar freestream Mach numbers. For the tunnel nozzle cases, the PSD is computed about x = 3.3 m and z = 0 m.

Figures 11 depicts the skewness of the temperature and pressure fluctuations from a quasi-2D nozzle DNS solution using the current grid described in Section II.A and Figure 2. The skewness is defined as the summation in time of an instantaneous system variable subtracted by the mean of that variable cubed divided by the number of snapshots and the standard deviation cubed. We define the kurtosis similarly, except for taking the fourth power instead of the third power. These calculations are performed at x = 3.3 m by using 54 and 82 instantaneous snapshots. We see from Figure

11 that the temperature skewness is close to convergence and contains two large symmetric peaks near the edges of the boundary layers. Notice that the pressure skewness is also relatively converged and reaches a maximum value in the freestream. This suggests that the statistics of the acoustic fluctuations have a noticeable departure from Gaussian behavior. There is also a very large gradient across the boundary layers in the pressure skewness. We do not show the kurtosis of the temperature and pressure. More instantaneous snapshots are needed to achieve better convergence of the higher-order statistics. It is important to note that we do see the same large symmetric peaks in the temperature kurtosis (that are also present in the temperature skewness).

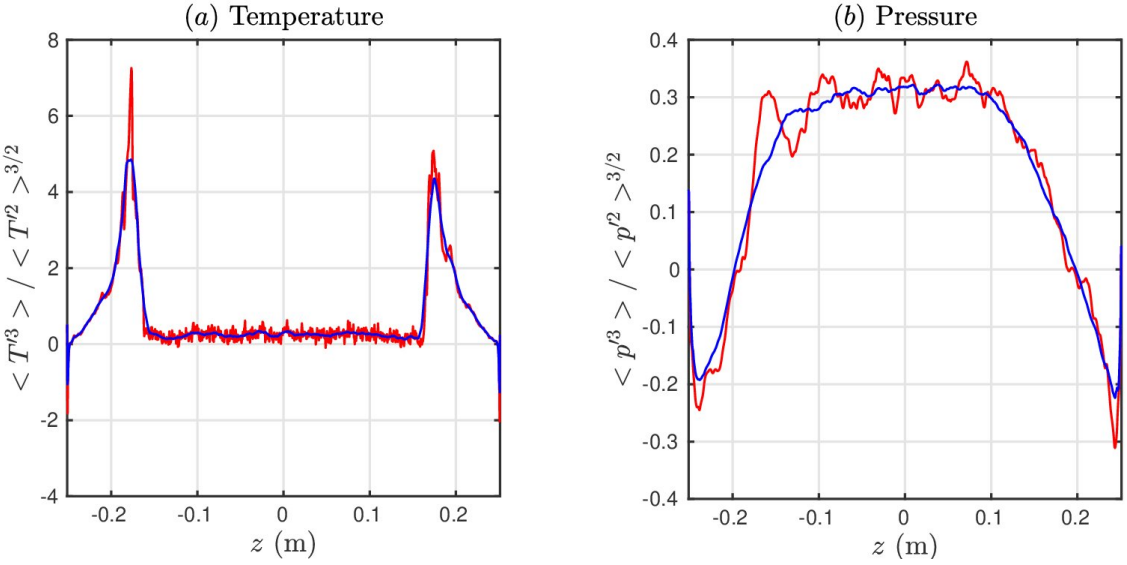

Fig. 11 Skewness of the (a) temperature and (b) pressure fluctuations at x = 3.3 m from a quasi-2D nozzle DNS solution using the current grid. Here, the blue line represents a solution computed with 82 instantaneous snapshots, while the red line denotes a solution computed with 54 snapshots.

To visualize the 3D flow field of the rectangular tunnel nozzle DNS solution with two turbulent boundary layers, we plot an instantaneous snapshot with color contours of Q-criterion isosurfaces and grayscale contours of density gradient magnitude in Figure 12. The spatial development of the two boundary layers can be seen in the Q-criterion isosurfaces. Notice that the two turbulent boundary layers grow at approximately the same rate. Acoustic fluctuations radiating from both turbulent boundary layers at angles ranging from roughly 30 to 35 degrees [17] can be seen in the grayscale contours of the density gradient magnitude on an xz-plane.

Along with running quasi-2D nozzle simulations that have two turbulent boundary layers, we also performed a simulation that has only one turbulent boundary layer (developing on the bottom wall). To obtain this DNS solution, we turned off the digital-filter-based synthetic turbulence injection method that generates correlated random fluctuations along the top portion of the left inlet. Grayscale contours of the density gradient magnitude on an xz-plane from the DNS with only one turbulent boundary layer is shown in Figure 13. Notice in Figure 13 that acoustic fluctuations are radiating from the bottom wall and not the top wall. This differs from Figure 12, which shows acoustic fluctuations radiating from both walls due to the turbulence that is generated by the top and bottom boundary layers. We plot the root-mean-square pressure fluctuation field divided by the wall shear stress induced by the turbulent boundary layer over the bottom nozzle wall in Figure 9 for all three tunnel nozzle simulations. The values of $p_{\text{rms}}/\tau_{\text{w}}$ versus z_n from the DNS that has only one turbulent boundary layer agrees much better with the separate flat-plate calculations [9, 14, 25] than the simulations that have two turbulent boundary layers. This result is expected because the separate flat-plate calculations have only one turbulent boundary layer by definition.

IV. Conclusion

We performed direct numerical simulations of the acoustic radiation in a quasi-2D rectangular nozzle test section to further understand the wind-tunnel acoustic environment in nonaxisymmetric nozzles. This work is also an extension of the earlier work by Deegan et al. [17], which presented preliminary simulations of the acoustic radiation in a quasi-2D

nozzle by using a coarser computational mesh, especially in the contoured part of the nozzle upstream of the test section. Comparisons of the centerline Mach number, boundary-layer thickness, Reynolds stresses, boundary-layer profiles, and root-mean-square pressure fluctuation fields between the simulations presented in this work and in Ref. [17] all resulted in good agreement. We also compared the Reynolds- and Favre-averaged stresses at three different streamwise locations, which seemed to indicate relatively good agreement both inside and outside the boundary layer. By suppressing the effects of the spanwise end walls and the corners on the acoustic noise generation, the simpler quasi-2D flow configuration proved useful in characterizing the effects of the individual wind-tunnel walls on the overall acoustic disturbance field and provided a less expensive means of fine tuning the simulation process for the eventual fully-3D simulation that includes the end walls. Furthermore, the good comparisons of the statistics of the nozzle-wall boundary-layer turbulence and of the freestream acoustic disturbances between the simulations of coarser and finer grids confirms both the adequacy of the DNS procedure and the insensitivity of the noise characteristics in the test section to the inflow turbulence generation technique.

This paper also presented the results from a simulation that had only one turbulent boundary layer along the bottom nozzle wall (instead of both along the top and bottom walls). The cross-stream variation of the root-mean-square pressure fluctuation field divided by the wall shear stress induced by the turbulent boundary layer over the bottom nozzle wall in the case with only one turbulent boundary layer agreed well with several flat-plate calculations [9, 14, 25]. An instantaneous snapshot with grayscale contours of density gradient magnitude shows the strong impact a turbulent boundary layer has on generating freestream acoustic fluctuations.

Future work will focus on the effects that both spanwise end walls and corners have on the acoustic noise generation and reverberation processes in a rectangular nozzle test section.

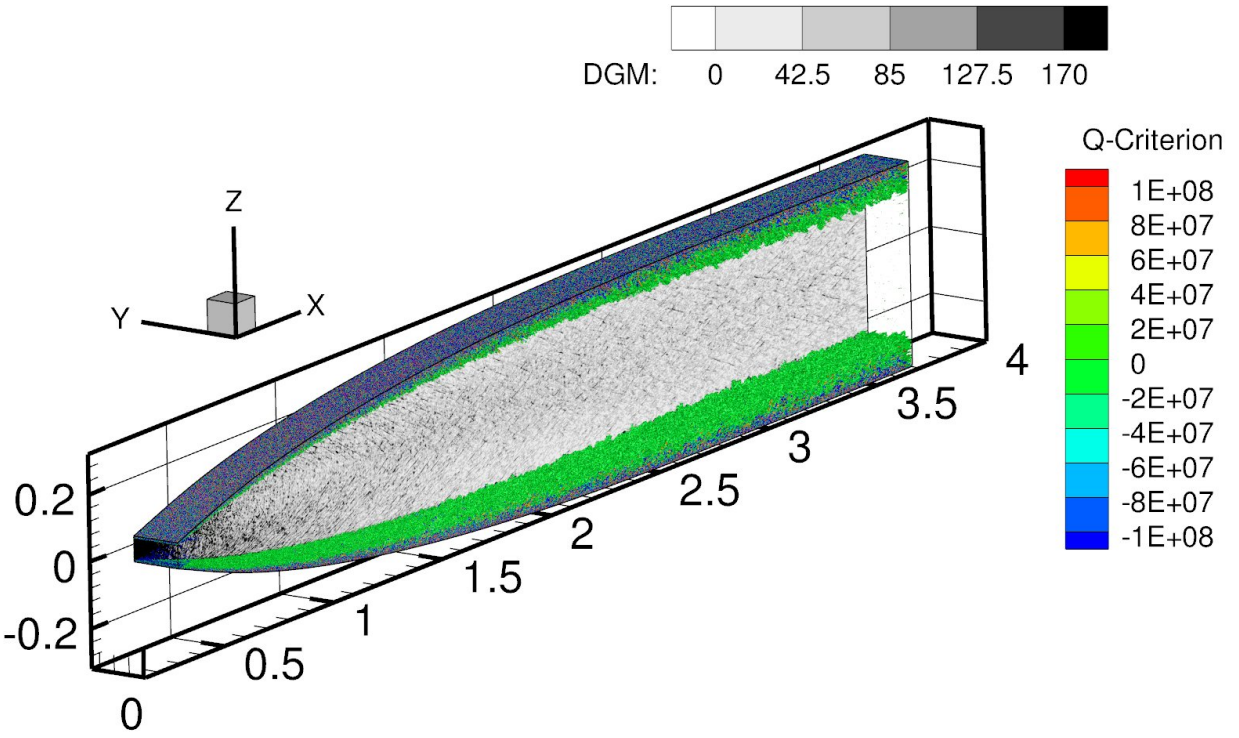

Fig. 12 An instantaneous snapshot with color contours of Q-criterion isosurfaces and grayscale contours of Density Gradient Magnitude (DGM). This snapshot corresponds to a quasi-2D nozzle DNS solution using the current grid with two turbulent boundary layers. Similar to Deegan et al. [17], the nozzle shape has been nonuniformly distorted from its actual contour.

Acknowledgments

This work is performed as part of the Hypersonic Technology (HT) project of the NASA Advanced Air Vehicles Program (AAVP). Computational resources supporting this work are provided by the NASA High-End Computing (HEC)

program through the NASA Advanced Supercomputing (NAS) Division at Ames Research Center. One of the authors (L. Duan) would like to acknowledge financial support by the Office of Naval Research under grant N00014-17-1-2347, managed by Dr. Eric Marineau.

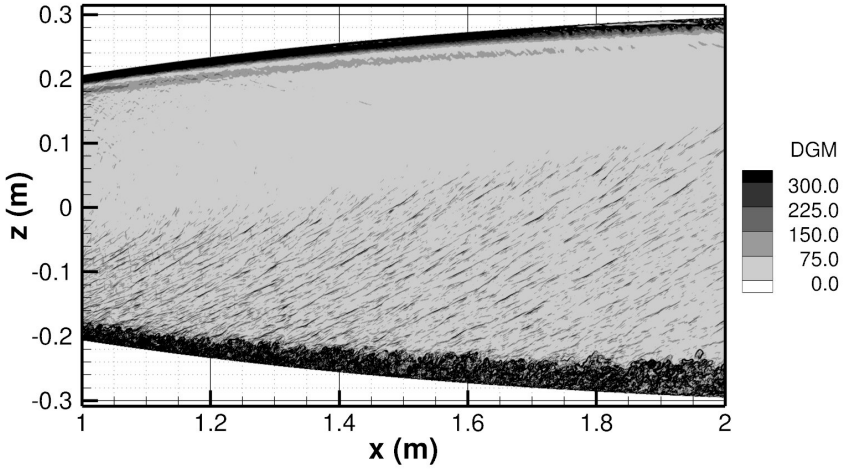

Fig. 13 An instantaneous snapshot with grayscale contours of DGM on an xz-plane corresponding to a quasi-2D nozzle DNS solution using the current grid, but with only one turbulent boundary layer instead of two. Similar to Deegan et al. [17], the nozzle shape has been nonuniformly distorted from its actual contour.

References

[1] White, F. M., *Viscous Fluid Flow*, McGraw-Hill, 2006.

[2] Morkovin, M. V., "On Transition Experiments at Moderate Supersonic Speeds," *Journal of the Aeronautical Sciences*, Vol. 24, No. 7, 1957, pp. 480–486.

[3] Laufer, J., "Aerodynamic Noise in Supersonic Wind Tunnels," *Journal of the Aeronautical Sciences*, Vol. 28, No. 9, 1961, pp. 685–692.

[4] Laufer, J., "Some Statistical Properties of the Pressure Field Radiated by a Turbulent Boundary Layer," *Physics of Fluids*, Vol. 7, No. 8, 1964, pp. 1191–1197.

[5] Pate, S. R., "Measurements and Correlations of Transition Reynolds Numbers on Sharp Slender Cones at High Speeds," *AIAA Journal*, Vol. 9, No. 6, 1971, pp. 1082–1090.

[6] Stetson, K. F., "Nosetip Bluntness Effects on Cone Frustum Boundary-Layer Transition in Hypersonic Flow," AIAA Paper 1983-1763, 1983.

[7] Fedorov, A. V., "Receptivity of a High-Speed Boundary Layer to Acoustic Disturbances," *Journal of Fluid Mechanics*, Vol. 491, 2003, pp. 101–129.

[8] Zhong, X., and Wang, X., "Direct Numerical Simulation on the Receptivity, Instability, and Transition of Hypersonic Boundary Layers," *Annual Review of Fluid Mechanics*, Vol. 44, 2012, pp. 527–561.

[9] Duan, L., Choudhari, M. M., Chou, A., Munoz, F., Ali, S. R. C., Radespiel, R., Schilden, T., Schröder, W., Marineau, E. C., Casper, K. M., Chaudhry, R. S., Candler, G. V., Gray, K. A., and Schneider, S. P., "Characterization of Freestream Disturbances in Conventional Hypersonic Wind Tunnels," *Journal of Spacecraft and Rockets*, Vol. 56, No. 2, 2019, pp. 357–368.

[10] Donaldson, J., and Coulter, S., "A Review of Free-Stream Flow Fluctuation and Steady-State Flow Quality Measurements in the AEDC/VKF Supersonic Tunnel A and Hypersonic Tunnel B," AIAA Paper 1995-6137, 1995.

[11] Schneider, S. P., "Effects of High-Speed Tunnel Noise on Laminar-Turbulent Transition," *Journal of Spacecraft and Rockets*, Vol. 38, No. 3, 2001, pp. 323–333.

[12] Duan, L., Choudhari, M. M., and Wu, M., "Numerical Study of Acoustic Radiation Due to a Supersonic Turbulent Boundary Layer," *Journal of Fluid Mechanics*, Vol. 746, 2014, pp. 165–192.

[13] Duan, L., and Choudhari, M. M., "Analysis of Numerical Simulation Database for Pressure Fluctuations Induced by High-Speed Turbulent Boundary Layers," AIAA Paper 2014-2912, 2014.

[14] Duan, L., Choudhari, M. M., and Zhang, C., "Pressure Fluctuations Induced by a Hypersonic Turbulent Boundary Layer," *Journal of Fluid Mechanics*, Vol. 804, 2016, pp. 578–607.

[15] Huang, J., Zhang, C., Duan, L., and Choudhari, M. M., "Direct Numerical Simulation of Hypersonic Turbulent Boundary Layers inside an Axisymmetric Nozzle," AIAA Paper 2017-0067, 2017.

[16] Huang, J., Duan, L., and Choudhari, M. M., "Direct Numerical Simulation of Acoustic Noise Generation from the Nozzle Wall of a Hypersonic Wind Tunnel," AIAA Paper 2017-3631, 2017.

[17] Deegan, C. P., Duan, L., and Choudhari, M. M., "Direct Numerical Simulation of Acoustic Disturbances in the Rectangular Test Section of a Hypersonic Wind Tunnel," AIAA Paper 2018-3219, 2018.

[18] Wu, M., and Martín, M. P., "Direct Numerical Simulation of Supersonic Turbulent Boundary Layer over a Compression Ramp," *AIAA Journal*, Vol. 45, No. 4, 2007, pp. 879–889.

[19] Jiang, G.-S., and Shu, C.-W., "Efficient Implementation of Weighted ENO Schemes," *Journal of Computational Physics*, Vol. 126, No. 1, 1996, pp. 202–228.

[20] Taylor, E. M., Wu, M., and Martín, M. P., "Optimization of Nonlinear Error Sources for Weighted Essentially Non-Oscillatory Methods in Direct Numerical Simulations of Compressible Turbulence," *Journal of Computational Physics*, Vol. 223, No. 1, 2006, pp. 384–397.

[21] Williamson, J. H., "Low-Storage Runge-Kutta Schemes," *Journal of Computational Physics*, Vol. 35, No. 1, 1980, pp. 48–56.

[22] Touber, E., and Sandham, N. D., "Oblique Shock Impinging on a Turbulent Boundary Layer: Low-Frequency Mechanisms," AIAA Paper 2008-4170, 2008.

[23] Dhamankar, N. S., Martha, C. S., Situ, Y., Aikens, K. M., Blaisdell, G. A., Lyrintzis, A. S., and Li, Z., "Digital Filter-Based Turbulent Inflow Generation for Jet Aeroacoustics on Non-Uniform Structured Grids," AIAA Paper 2014-1401, 2014.

[24] Thompson, K. W., "Time Dependent Boundary Conditions for Hyperbolic Systems," *Journal of Computational Physics*, Vol. 68, No. 1, 1987, pp. 1–24.

[25] Zhang, C., Duan, L., and Choudhari, M. M., "Effect of Wall Cooling on Boundary Layer Induced Pressure Fluctuations at Mach 6," *Journal of Fluid Mechanics*, Vol. 822, 2017, pp. 5–30.

[26] van Driest, E. R., "The Problem of Aerodynamic Heating," *Aeronautical Engineering Review*, Vol. 15, No. 10, 1956, pp. 26–41.

[27] Trettel, A., and Larsson, J., "Mean Velocity Scaling for Compressible Wall Turbulence with Heat Transfer," *Physics of Fluids*, Vol. 28, No. 026102, 2016.

[28] Huang, P. G., Coleman, G., and Bradshaw, P., "Compressible Turbulent Channel Flows: DNS Results and Modelling," *Journal of Fluid Mechanics*, Vol. 305, 1995, pp. 185–218.